

Journal of Geophysical Research: Solid Earth

RESEARCH ARTICLE

10.1002/2017JB015019

Key Points:

- 2-D ambient noise adjoint tomography technique for linear arrays was developed
- 3-D/2-D transformation for converting observed surface wave data in 3-D media to the reconstructed data in 2-D media was performed
- Low-velocity zone in the lower crust and gradual velocity change, suggesting intense crust-mantle interactions in North China Craton, was revealed

Supporting Information:

- Supporting Information S1

Correspondence to:

H. Yao,
hjyao@ustc.edu.cn

Citation:

Zhang, C., Yao, H., Liu, Q., Zhang, P., Yuan, Y. O., Feng, J., & Fang, L. (2018). Linear array ambient noise adjoint tomography reveals intense crust-mantle interactions in North China craton. *Journal of Geophysical Research: Solid Earth*, 123, 368–383. <https://doi.org/10.1002/2017JB015019>

Received 22 SEP 2017

Accepted 9 DEC 2017

Accepted article online 15 DEC 2017

Published online 9 JAN 2018

Linear Array Ambient Noise Adjoint Tomography Reveals Intense Crust-Mantle Interactions in North China Craton

Chao Zhang^{1,2}, Huajian Yao¹ , Qinya Liu^{2,3} , Ping Zhang¹, Yanhua O. Yuan⁴, Jikun Feng¹ , and Lihua Fang⁵ 

¹Laboratory of Seismology and Physics of Earth's Interior, School of Earth and Space Sciences, University of Science and Technology of China, Hefei, China, ²Department of Physics, University of Toronto, Toronto, Ontario, Canada, ³Department of Earth Sciences, University of Toronto, Toronto, Ontario, Canada, ⁴Department of Geosciences, Princeton University, Princeton, NJ, USA, ⁵Institute of Geophysics, China Earthquake Administration, Beijing, China

Abstract We present a 2-D ambient noise adjoint tomography technique for a linear array with a significant reduction in computational cost and show its application to an array in North China. We first convert the observed data for 3-D media, i.e., surface-wave empirical Green's functions (EGFs) to the reconstructed EGFs (REGFs) for 2-D media using a 3-D/2-D transformation scheme. Different from the conventional steps of measuring phase dispersion, this technology refines 2-D shear wave speeds along the profile directly from REGFs. With an initial model based on traditional ambient noise tomography, adjoint tomography updates the model by minimizing the frequency-dependent Rayleigh wave traveltimes between the REGFs and synthetic Green functions calculated by the spectral-element method. The multitaper traveltime difference measurement is applied in four-period bands: 20–35 s, 15–30 s, 10–20 s, and 6–15 s. The recovered model shows detailed crustal structures including pronounced low-velocity anomalies in the lower crust and a gradual crust-mantle transition zone beneath the northern Trans-North China Orogen, which suggest the possible intense thermo-chemical interactions between mantle-derived upwelling melts and the lower crust, probably associated with the magmatic underplating during the Mesozoic to Cenozoic evolution of this region. To our knowledge, it is the first time that ambient noise adjoint tomography is implemented for a 2-D medium. Compared with the intensive computational cost and storage requirement of 3-D adjoint tomography, this method offers a computationally efficient and inexpensive alternative to imaging fine-scale crustal structures beneath linear arrays.

1. Introduction

Surface wave data obtained from ambient noise and earthquakes can be used to resolve structures in the crust and upper mantle, on both global and regional scales (e.g., Lin et al., 2008; Shapiro et al., 2004; Simons et al., 1999; Yang et al., 2007; Yao et al., 2008). At the same time, shorter period surface waves have also been used to investigate shallow crustal or near surface velocity structures (e.g., Fang et al., 2015; Huang et al., 2010; Lin et al., 2013; Li et al., 2016; Shirzad & Shomali, 2014). However, most of these studies employed the so-called traditional ambient noise tomography method based on ray theory, which does not consider complex wave propagation phenomena in heterogeneous media. This results in seismic images with less accurate anomaly patterns and amplitudes. Recent advances in numerical methods for the wave equation combined with developments in high-performance computation (HPC) have enabled routine simulation of seismic wave propagation in realistic 2-D and 3-D Earth models based on the spectral-element method (SEM) (Komatsitsch et al., 2004; Komatsitsch & Tromp, 2002a, 2002b). Utilizing these seismic wave simulations, adjoint-state methods can efficiently incorporate the full nonlinearity of wave propagation in iterative seismic inversions (e.g., Bozdag et al., 2016; Chen et al., 2015, 2017; Fichtner & Villaseñor, 2015; Fichtner et al., 2009, 2010; Liu & Gu, 2012; Liu & Tromp, 2006, 2008; Tape et al., 2009, 2010; Tromp et al., 2005; Zhu et al., 2012; Zhu & Tromp, 2013; Zhu et al., 2015). Based on these advances, Chen et al. (2014) and Liu et al. (2017) proposed ambient noise adjoint tomography for 3-D crustal structures by matching the empirical Green function (EGF) and synthetic Green function (SGF) calculated based on SEM. Also, full-wave 3-D ambient noise tomography has been developed to image the structure of the Cascades, the Ontong Java Plateau, and the eastern North American margin (Covellone et al., 2015; Gao & Shen, 2014, 2015; Savage et al., 2017).

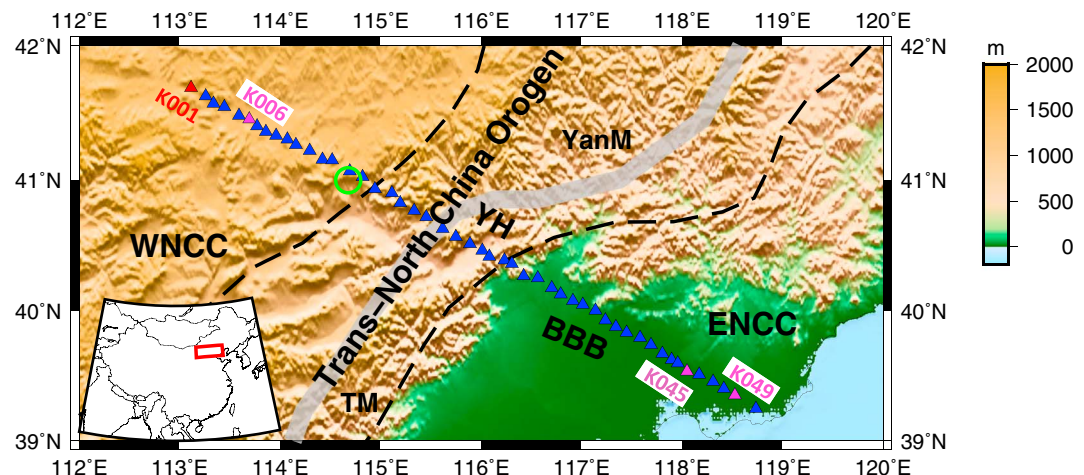


Figure 1. Topography and tectonic map of the study region in the North China Craton, modified after Zhao et al. (2005) and distribution of linear array stations (blue triangles). The black dashed lines outline the Trans-North China Orogen (TNCO). The thick gray half transparent line represents the North–South Gravity Lineament (NSGL). The green hollow circle denotes location of Cenozoic basalt bearing xenoliths in Hannuoba. Major tectonic units are also labeled, including the Yan Mountains (YanM), Taihang Mountains (TM), Yanqing-Huailai Basin (YH), and Bohai Bay Basin (BBB). The linear array consists of 49 stations, and the average of station spacing is approximately 10 km. Virtual source station K006 and receiver stations (K045 and K049), marked by purple triangles, will be used to show the waveform fitting between the reconstructed empirical Green's Functions (REGFs) and synthetic Green's functions (SGFs) in the following parts. The red triangle denotes the virtual source station K001, which will be used to show one example for 3-D/2-D transformation.

However, the computational cost and storage requirement of 3-D adjoint tomography are intensive (Bozdag et al., 2016; Zhu et al., 2015). In comparison, 2-D full waveform inversion (FWI) is computationally more efficient, preferential for code development and applications. It has been fully developed by oil industry in the past three decades, while 2-D elastic FWI has been applied to shallow surface waves recently (Dokter et al., 2014; Groos, 2013; Nuber et al., 2015; Romdhane et al., 2011; Tran et al., 2013). In particular, Forbriger et al. (2014), Schäfer et al. (2014), and Groos et al. (2017) proposed a stable workflow for 2-D FWI of shallow-seismic Rayleigh waves not only for synthetic data but also for real field-recorded data, in which a 3-D/2-D transformation scheme is developed to simulate the response to a line source (i.e., spreading correction) for shallow seismic surface waves. As more linear arrays with dense station spacing are deployed around the globe, this transformation also makes it possible to apply 2-D FWI to ambient noise data recorded by linear arrays.

In this paper, we present a 2-D adjoint tomography technique applied to ambient noise data recorded on a densely spaced linear array in North China. The North China Craton (NCC) is unique among cratons worldwide because of the unusual Mesozoic destruction of its cratonic lithosphere (Carlson et al., 2005). It consists of two major Archean blocks, the eastern (ENCC) and western NCC (WNCC), separated by the Paleoproterozoic Trans-North China Orogen (TNCO) (Zhao & Liu, 2001; Zhao et al., 2005), which marks variations in both surface topography and gravity anomalies (Figure 1). In contrast to its western part, which seems to have retained the cratonic nature and stability since Precambrian (Zhai & Liu, 2003), the eastern NCC underwent significant tectonic reactivation during the Late Mesozoic and Cenozoic (Fan et al., 2000; Griffin et al., 1998; Menzies et al., 1993; Wu et al., 2005; Xu, 2001), with both the lithospheric mantle (Chen, 2010) and the crust (Gao et al., 2004) being severely modified and thinned. Recent studies also suggest that localized lithospheric modification and thinning may also have taken place in the TNCO (Chen, 2010). From the late Mesozoic to Cenozoic, the TNCO is highlighted by episodic extension, rifting (Ren et al., 2002), and voluminous magmatic activities that are associated with the Hannuoba Neogene granulite and peridotite xenolith-bearing basalts in its northern margin (green circle in Figure 1). Given the complex tectonic setting, dynamic processes and mechanism of craton destruction in the NCC remain debatable.

Detailed seismic imaging of crust and upper mantle structures provides key insights into the Phanerozoic evolution of the TNCO and further contribute to understanding the geodynamic processes

driving localized lithospheric modification in this region (e.g., Duan et al., 2016; Fang et al., 2010; Fu et al., 2015; Jiang et al., 2013; Zhao et al., 2009; Zheng et al., 2008). Zheng et al. (2008) resolved a thick crust-mantle transition zone in the northern NCC using waveform inversion of P wave receiver function, which was interpreted as the seismic evidence on the possible magmatic underplating due to asthenospheric mantle upwelling. Zhao et al. (2009) observed a plume-like low-velocity anomaly in the upper mantle beneath the TNCO using finite frequency body wave tomography. Fang et al. (2010) observed middle and lower crustal low-velocity anomalies in the TNCO from dense array ambient noise tomography. Surface wave tomographic study by Jiang et al. (2013) also resolved a prominent low-velocity anomaly that extends to depths greater than 200 km in the northern TNCO. Recently, Fu et al. (2015) refined the low-velocity anomaly beneath the Fenhe Graben and Taihang Mountain, which originates from the lower crust to about 140 km depths. In addition, Duan et al. (2016) integrated previous 42 deep seismic sounding profiles over decades and provided a 3-D P wave velocity model in the central-eastern NCC (*HBCrust1.0*), but their model is relatively smooth and small-scale features are not well resolved. The overall features of these tomographic models are consistent, but the details do vary significantly, due largely to differences in imaging methods and inherent method limitations, as well as data coverage. Especially, detailed knowledge of the low-velocity anomaly at the crustal scale is still lacking. The developed 2-D adjoint tomography using ambient noise data from a dense linear array in this paper thus offers a new and reliable technique to constrain the detailed crustal structures in this region.

The paper is organized as follows. First, we give a short description of the array data and ambient noise cross-correlation method, then we briefly review the 3-D/2-D transformation method for surface-wave conversion. Next we describe our 2-D adjoint tomography workflow for ambient noise data recorded on the linear array. Afterward, we obtained the final shear velocity model, which reveals two striking new features, including a low-velocity zone in the lower crust and a gradual velocity change across the Moho beneath the junction of Taihang Mountains and Yin-Yan Mountains in the TNCO. Finally, we give a possible mechanism to explain these features, which mainly involves thermo-chemical interactions between mantle-derived upwelling melts and the lower crust.

2. Data

The continuous vertical-component seismograms, recorded by an array from January 2007 to February 2008 in the North China, are used in this study. This array consists of 49 stations, which starts at the eastern portion of the Bohai Bay Basin, crosses the Taihang Mountains in the middle, and ends at the interior of the Ordos Basin toward the west, traversing all the three constituent parts of the NCC (Figure 1). These stations are part of the 2-D dense temporary seismic array deployment in the eastern NCC (ChinArray, 2006), and the average station spacing is approximately 10 km. It can be completely considered as a linear array after analyzing the distribution of stations by linear regression (see detail on Figure S1 in the supporting information). Data are processed based on a procedure that is similar to that described in Bensen et al. (2007). Here we summarize it briefly. For each station, data are first cut into daily length after being decimated to 5 Hz with mean and linear trend removed. Then all of the daily segments are corrected for instrument response. Afterward, continuous records are spectrally whitened and then temporally normalized using the running-absolute-mean method to suppress the effects of nonstationary signals, especially earthquake signals. Next, all available daily traces are cross correlated between all station pairs to obtain noise cross-correlation functions (NCFs) and all daily correlations for the same station pair are normalized and linearly stacked. Finally, the positive and negative sides of each stacked NCF are further folded and summed to obtain the final NCF.

For a given station pair 1 and 2, the mutual relationship between the final NCF, the surface wave empirical Green's function (EGF), and the real Green's function (GF) can be represented as

$$\hat{G}_{12}(t) = -\frac{dC_{12}(t)}{dt} \approx G_{12}(t) \quad (1)$$

Here $C_{12}(t)$, $G_{12}(t)$, and $\hat{G}_{12}(t)$ are the folded NCF, the real GF, and the EGF, respectively (e.g., Lin et al., 2008; Yao & van der Hilst, 2009; Yao et al., 2006). The EGF is an approximation to the exact Green's function, which is

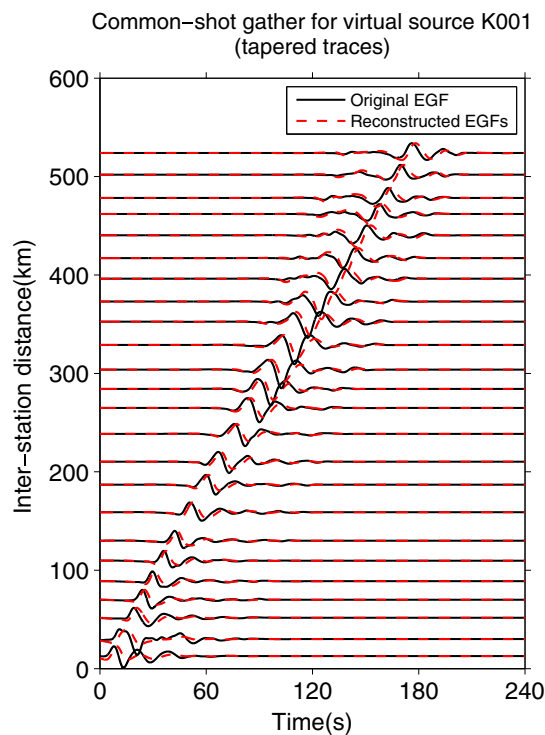


Figure 2. Comparison of original EGFs (black solid line) and reconstructed EGFs (red dash line) for virtual source K001 (marked as the red triangle in Figure 1). Each trace is normalized to its maximum amplitude and only every other trace is displayed.

subject to frequency-dependent amplitude corrections (Roux et al., 2005; Weaver & Lobkis, 2004) and errors due to, for instance, uneven distribution of ambient noise sources (Harmon et al., 2010; Yao & van der Hilst, 2009). To avoid near-field complexities of surface wave propagation, the interstation distance d is selected to be larger than twice of the average wavelength λ for each period band, that is,

$$d > 2\lambda = 2\bar{C}T \quad (2)$$

where \bar{C} is the average phase velocity and T is the maximum period within a frequency band.

3. 3-D/2-D Transformation

The surface wave EGFs obtained in our study corresponding to surface wave propagation between virtual sources (i.e., master stations) and receiver stations in a 3-D medium, which clearly differ in amplitude and phase from the surface waves generated by a line source in a 2-D medium. Thus, a 3-D/2-D transformation must be applied to the EGFs in 3-D prior to inversions in 2-D. In this study, we adopt the 3-D/2-D transformation method proposed for shallow-seismic surface waves (Forbriger et al., 2014; Schäfer et al., 2014). This 3-D/2-D transformation is based on the Green's functions for the 3-D and 2-D acoustic wave equation, but it is also shown to be reasonable for elastic seismic waves. First, each trace of EGFs in 3-D is convolved with $\sqrt{1/t}$, which corresponds to a phase shift of $\pi/4$. Afterward, each trace is tapered at both sides in order to suppress phases other than the fundamental mode Rayleigh waves. Furthermore, an amplitude factor F_{amp} is applied to each trace, which corrects the surface-wave amplitudes (see Text S1 for details).

To demonstrate the accuracy of 3-D/2-D transformation, we perform a synthetic 2-D test. The 2-D test model comes from the initial model used in our 2-D ambient noise adjoint tomography. The shear velocity, compressional velocity, and density models are displayed in Figure S2. For point-source simulations, the 2.5-D model is constructed by the 2-D model uniformly extending over 100 km in the third spatial dimension perpendicular to the profile. We calculate wavefields excited by the point source and line source, with SPECFEM3D and SPECFEM2D, respectively. A Gaussian pulse with a dominant source frequency of 0.5 Hz is used as the source time function. The computing time for the 3-D and 2-D modeling are shown in Table S1. The test results show that this transformation performs excellently for our synthetic case, as detailed in the Text S2 and Figure S3. Similarly, we apply this transformation to field data (i.e., the original EGFs in 3-D media) to obtain the reconstructed EGFs (REGFs) for 2-D media. Figure 2 shows a comparison of the traces generated by the virtual source station K001 (marked as the red triangle in Figure 1) before and after 3-D/2-D transformation. The phase shift of $\pi/4$ can be observed between the EGFs and REGFs.

4. 2-D Ambient Noise Adjoint Tomography

We adopt the technique of adjoint tomography to invert for 2-D shear wave speed using ambient noise data recorded on a linear array in North China. A vertical point force with Gaussian source time function with dominant frequency of 0.5 Hz is set at 1 km depth beneath each station as the virtual source to generate 2-D synthetic Green's functions (SGFs), which are computed by a 2-D spectral-element code, SPECFEM2D.

4.1. Misfit Function

We measure the frequency-dependent traveltime misfits between the REGFs and SGFs using the multitaper method (Zhou et al., 2004). The measurements are divided into a number of categories, i.e., traveltime

measurements from four period bands. The frequency-dependent traveltime misfit in each category c (that is, each period band) may be expressed as

$$\chi_c = \frac{1}{N_c} \sum_{s=1}^{N_s} \sum_{i=1}^{N_c^s} \int w_i(\omega) \left[\frac{\Delta T_i(\omega)}{\sigma_i} \right]^2 d\omega / \int w_i(\omega) d\omega \quad (3)$$

Here the quantities ΔT_i and σ_i are frequency-dependent phase differences in frequency window w_i and associated uncertainty for multitaper measurements, respectively. N_c^s denotes the number of measurements in category c for source s , N_s is the total number of sources, and $N_c = \sum_{s=1}^{N_s} N_c^s$ is the total number of measurements in category c . If multitaper measurements cannot be made on a trace, we use cross-correlation measurements instead. Thus, the total misfit for all categories is given by

$$\chi_{\text{all}} = \frac{1}{C} \sum_{c=1}^C \chi_c \quad (4)$$

Here C is the number of period bands, which is 4 in this study.

4.2. Model Parameterization

Following the standard procedures of adjoint tomography for ambient noise data (Chen et al., 2014; Liu et al., 2017), we perform one adjoint simulation by simultaneously injecting back adjoint sources at all virtual receiver stations into the model for each virtual source station. This creates an adjoint wavefield s^\dagger . The time integration of the interaction of s^\dagger and the forward wavefield s yields the event sensitivity kernels. Perturbations in the overall travelttime misfit $\delta\chi(m)$ is linearly related to relative perturbations in density $\delta \ln \rho$, P wave velocity $\delta \ln \alpha$, and S wave velocity $\delta \ln \beta$:

$$\delta\chi = \int (K_\rho \delta \ln \rho + K_\alpha \delta \ln \alpha + K_\beta \delta \ln \beta) d^2x \quad (5)$$

where K_ρ , K_α , and K_β are the corresponding Fréchet kernels for these three structure parameters. We ignore attenuation in this study but focus on refining the elastic 2-D structure. In general, surface wave dispersion is mostly sensitive to shear wave speed. However, short period Rayleigh wave dispersion also has a significant sensitivity to compressional wave speed in the shallow crust. We relate compressional wave speed and density to shear wave speed using the empirical relationships (Brocher, 2005):

$$\alpha = \sum_n \chi_n^{[\alpha]} \beta^n \quad (6)$$

$$\rho = \sum_n \chi_n^{[\rho]} \alpha^n \quad (7)$$

Here $\chi_n^{[\alpha,\rho]}$ represent the fitting polynomial coefficients. Similar as Fang et al. (2015), we have

$$\delta \ln \alpha = \beta / \alpha \sum_n n \chi_n^{[\alpha]} \beta^{n-1} \delta \ln \beta = R_\alpha \delta \ln \beta \quad (8)$$

$$\delta \ln \rho = \alpha / \rho \sum_n n \chi_n^{[\rho]} \alpha^{n-1} \delta \ln \alpha = R_\rho \delta \ln \alpha \quad (9)$$

where $R_\alpha = \beta / \alpha \sum_n n \chi_n^{[\alpha]} \beta^{n-1}$, $R_\rho = \alpha / \rho \left(R_\alpha \sum_n n \chi_n^{[\rho]} \alpha^{n-1} \right)$. Finally, the misfit can be expressed as

$$\delta\chi = \int [(K_\rho R_\rho + K_\alpha R_\alpha + K_\beta) \delta \ln \beta] d^2x \quad (10)$$

Through equation (10) we explicitly include the kernels of compressional wave speed and density on the calculation of combined misfit kernel.

An isotropic 2-D initial shear speed model is extracted from an existing 3-D shear wave speed model by traditional ambient noise tomography (Fang et al., 2010), while the P wave velocity and density model are derived from the S wave velocity model according to the empirical functions (6) and (7). Generally, it is better to start from a smoothed model in waveform inversion. The smoothed initial model by a Gaussian filter is shown as Figure S2 in the supporting information. For convenience, the model is parameterized on the SEM Gauss-Lobatto-Legendre grid points. The simulation domain is 650 km \times 100 km, and the average grid spacing of mesh is 2.5 km. Also, 2 km topographic variations from the WNCC to the ENCC are incorporated in the mesh. The detailed numerical parameters of modeling are shown in Table 1.

Table 1*Numerical Parameters of Modeling and Core Hours Spent During the 14 Structural Iterations*

Model size ($N_x \times N_z$)	x-Direction: 650 km; z-direction: 100 km (300*40 elements)
Propagation time	12,000 time steps; Time discretization: 0.02 s
Number of processors for each source	4
Total number of CPUs/cores	196
Computing time for inversion	4.5 h

4.3. Period Band and Adaptive Window Selection.

We filter the REGFs and SGFs in four period bands: 20–35 s, 15–30 s, 10–20 s, and 6–15 s. **These overlapping period bands are designed to reduce the nonlinearity of inversion.** Examples of the filtered REGFs in different period bands are shown in Figure 3.

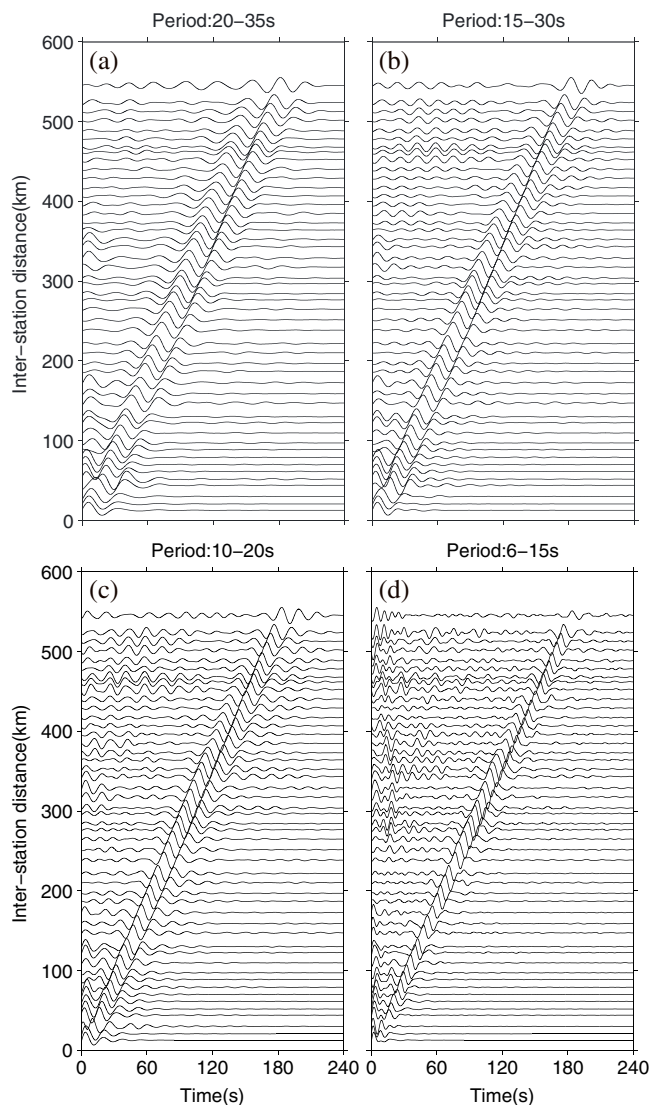


Figure 3. Reconstructed empirical Green's function (REGFs) waveforms derived from ambient noise interferometry between station K001 and the other stations in four different period ranges, (a) 20–35 s, (b) 15–30 s, (c) 10–20 s, and (d) 6–15 s, plotted with increasing inter-station distances.

As we only need to extract the Rayleigh wave, it is not necessary to use the FLEXWIN algorithm developed by Maggi et al. (2009). Instead, we propose an adaptive window selection approach for surface waves based on the average group velocity of each period range. As shown in Figure 4a, the envelope of SGF is first obtained by Hilbert transformation (red dashed line). Then, a Tukey window with a length of 5 times of the selected period is applied to the SGF (blue solid line) and REGFs (black solid line) centering at the maximum amplitude of the envelope (red point). The window length for short-period band will be much shorter than that of the long-period band to suppress other phases. For each selected window, we measure the frequency-dependent traveltime misfit between REGFs and SGFs using the multitaper method. Low-quality signals are removed from the measurements using a minimum signal-to-noise ratio of 10 and a minimum cross-correlation coefficient of 0.8. Table 2 lists the number of REGFs selected from the four period bands used in the inversion. Figure 4b displays an example of multitaper measurement made for four period bands. The corresponding adjoint sources for four period bands are shown in Figure 4c.

4.4. Inversion Strategy.

Once Fréchet derivatives related to all virtual sources are computed, the adjoint tomography workflow continues to a postprocessing phase and then a model update (Bozdag et al., 2016).

First, Fréchet derivatives of different virtual sources (i.e., event kernels) are summed to obtain the full gradient of the misfit function. Then 2-D Gaussian function is used to smooth the summed kernel as a regularization procedure (Tape et al., 2010; Zhu et al., 2015). The shape of the Gaussian function is determined by half widths in the horizontal and vertical directions, σ_x and σ_z . They are chosen based on the wavelengths of structures that can be potentially resolved by the current frequency bands. These two widths are reduced as the model improves. In this paper, σ_x is decreased from 30 km to 10 km, while σ_z is from 10 km to 5 km after 5 iterations, reflecting the incorporation of shorter period surface wave measurements. Next, the smoothed kernel is preconditioned by a preconditioner, which can be numerically calculated through the interaction between the forward and adjoint acceleration fields, namely, the pseudo-Hessian (Luo, 2012).

$$P(x) = H_{pp}^2(x, x) = \sum_{s=1}^{N_s} \int \partial_t^2 s(x, t) \cdot \partial_t^2 s^\dagger(x, T-t) dt \quad (11)$$

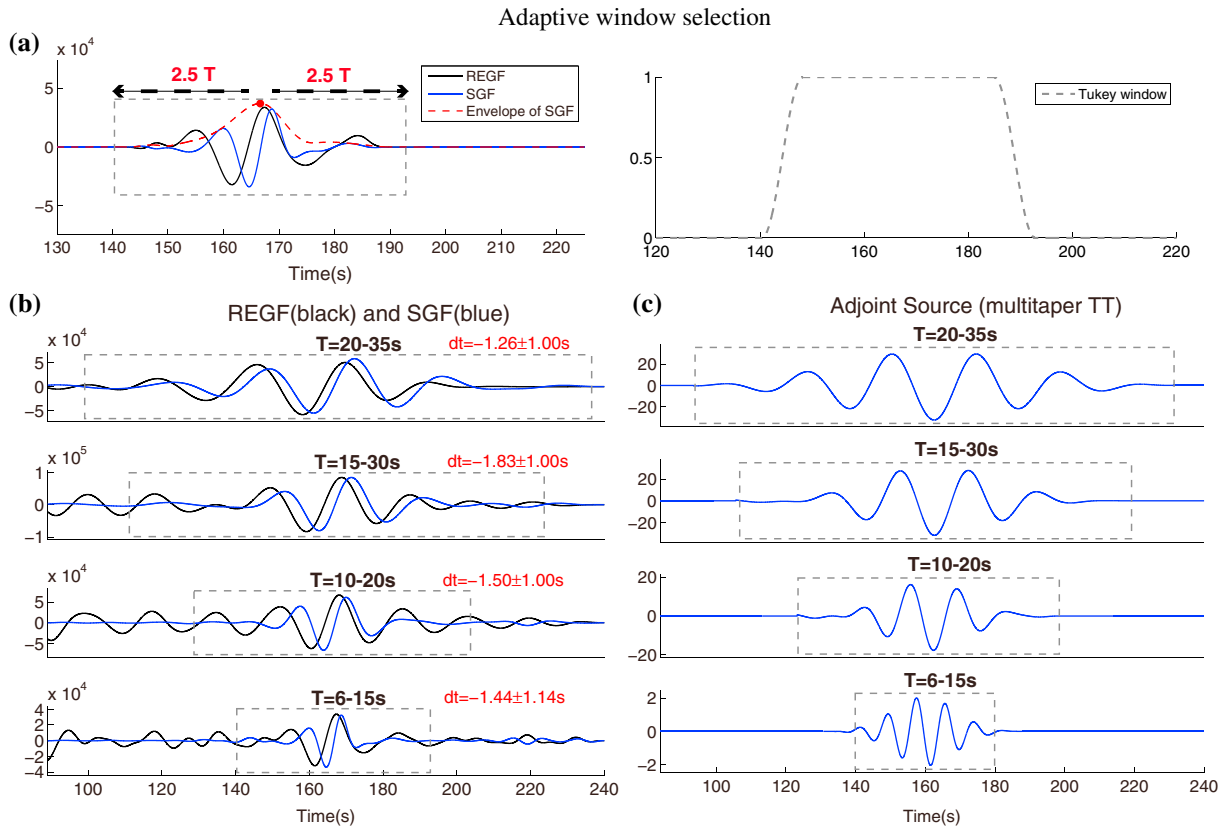


Figure 4. An example of station pair: K006–K049 (which are marked as purple triangles in Figure 1), to demonstrate how to choose the time window and measure the traveltime delay to generate the adjoint source; (a) Adaptive Tukey window for surface waves in different period bands: First, the envelope of SGFs is obtained by Hilbert transformation (red dash line), then the 5-T Tukey window is applied to the SGFs and REGFs centered at the maximum amplitude of the envelope (red point). The right plot shows the Tukey window used in the time domain. (b) SGFs (blue solid line), REGFs (black solid line), and waveform windows (gray dashed line) for different period bands (20–35 s, 15–30 s, 10–20 s, and 6–15 s). In the up-right corner, we list the multitaper traveltime difference as well as the uncertainty (by red words) for each period band. $dt = t_{\text{obs}} - t_{\text{syn}}$, where t_{obs} and t_{syn} are defined as the observed traveltime and synthetic traveltime, respectively. (c) Adjoint sources for multitaper traveltime measurements at each period band.

Here s and s^\dagger denote the forward and adjoint displacements, respectively, and N_s denotes the number of sources. Finally we use the L-BFGS method (Nocedal, 1980) to update the model. Following Chen et al. (2014), the optimal step length can be determined by minimizing the misfit calculated from a subset of virtual sources selected from a large number of stations. However, as there are only 49 stations in our case and 2-D SEM simulations are relatively fast, we decided to use all the stations in searching for the optimal step length. Specifically, we generate several test models by setting up different values of step length and evaluate the misfit for each test model. The model with the minimum value for the overall misfit is selected as the new model. Figure 5 shows how we select the optimal step length in the first iteration based on this strategy. The values of the step length ν are set to 1% to 5% in an increment of 1%. The evolution of overall misfit with increasing ν values is shown in Figure 5a, which is used to determine the optimal step, while the evolution of misfit for individual period bands are also shown in Figures 5b–5e. Once the optimal step length is determined from the minimum of the total function for all bands, the model parameters m may be updated via

$$\ln(m_{i+1}/m_i) = \nu_i d_i \quad (12)$$

where m_{i+1} and m_i are the model of the $(i+1)$ th iteration and the i th iteration. The ν_i and d_i are the optimal step length and the search direction (i.e., summed event kernels) from the i th iteration, respectively. Also, compressional wave speed and density will be updated each iteration via the same empirical function (6) and (7).

Table 2
Number of REGFs Used in the Inversion

Period(s)	Num.
20–35 s	492
15–30 s	618
10–20 s	803
6–15 s	418
All	2,331

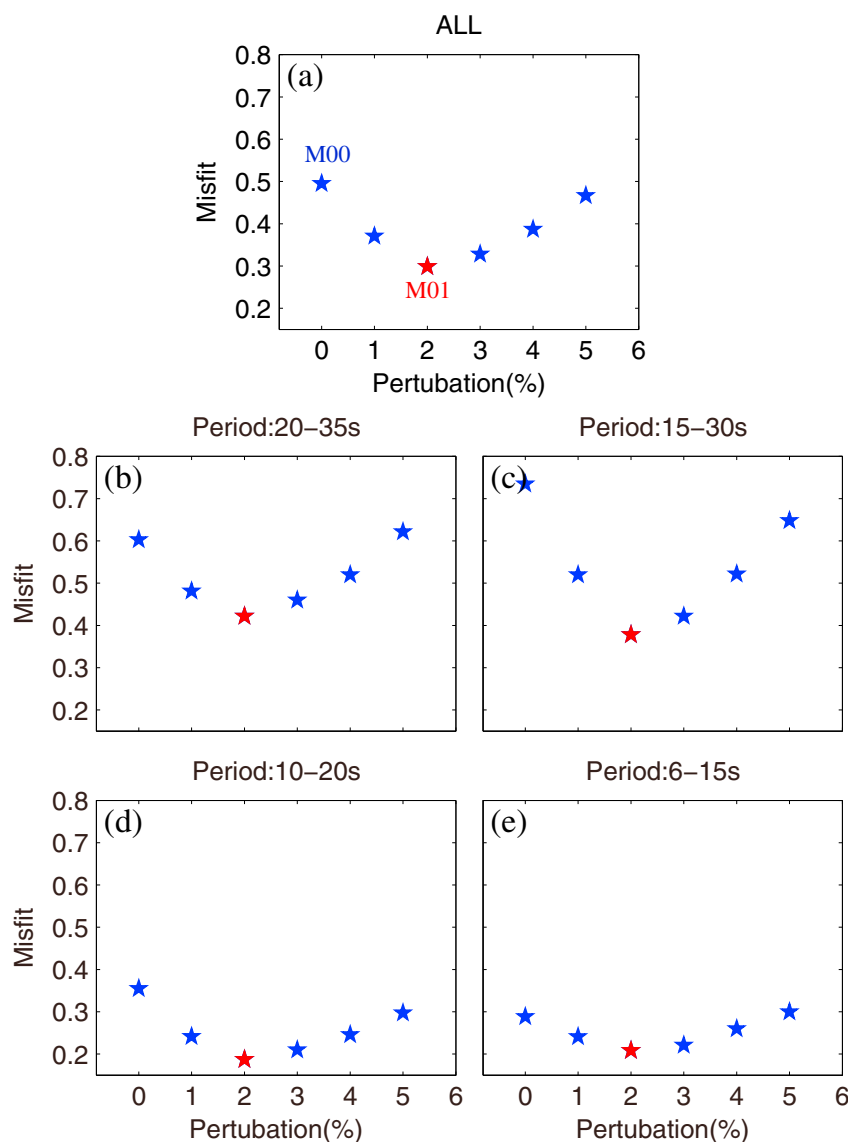


Figure 5. Line search to determine the step length for the first iteration. (a) Evolution of total misfit with different ν values ranging from 0 to 5% with an increment of 1%. (b–e) Evolution of misfit for four different period ranges: 20–35 s, 15–30 s, 10–20 s, and 6–15 s.

5. Results and Resolution Tests

Figure 6a shows the reduction of misfit function with increasing number of iteration. The final model shows a significant reduction in the misfit between the SGFs and REGFs not only for the overall misfits but also for the misfits for individual period bands. A “jump” in the misfit curve from M04 to M05 is due to the width change of Gaussian filter for kernels. The traveltime histograms for the initial model (M00) and the model after 14 iterations (M14) are shown in Figure 6b. We can see that (1) for M00, the average traveltime residuals dt (observed traveltime minus predicted time) for different period bands are negative, which means that the SGFs arrive later than REGFs. The seismograms in Figure 4b also show the similar trend. It suggests that the velocity of our initial model is relatively slower than the real Earth structure. (2) Upon our iterations, the traveltime residual drops from the initial -0.38 ± 0.61 s to the final 0.01 ± 0.33 s, where the average traveltime residual is very close to zero and the standard deviation has also a significant reduction. (3) The 99.4% of the traveltime residuals after inversion fall in the range from -1 to 1 s.

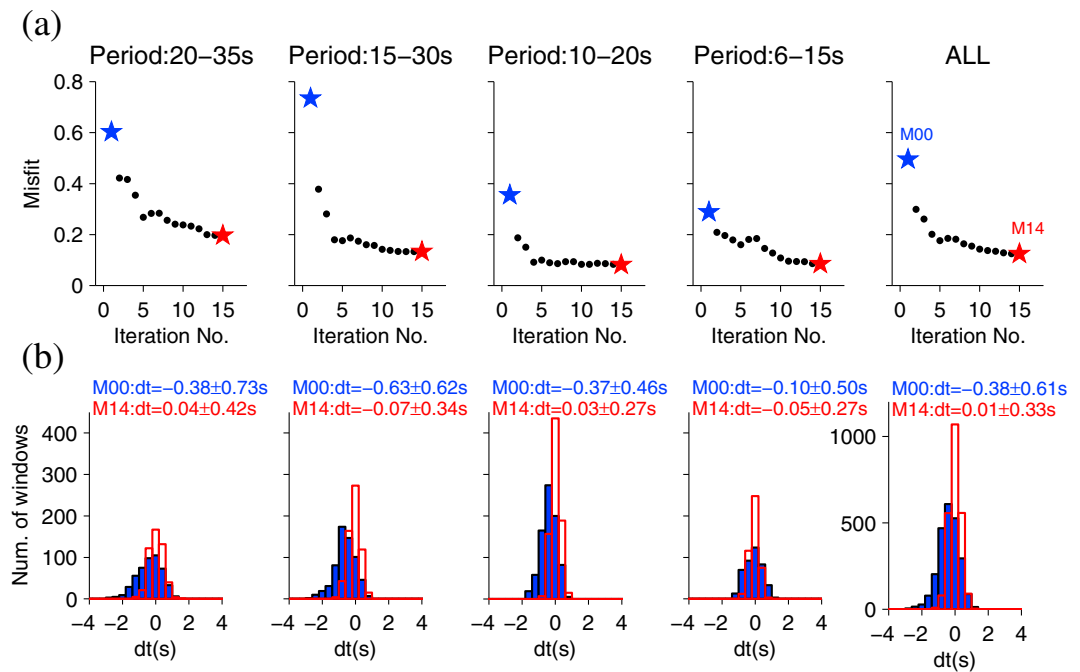


Figure 6. (a) Reduction of misfit function values as a function of iteration number not only for the overall misfits (ALL) but also for the misfits in different period bands. There is a jump in the misfit curve from model 4 to model 5 due to the decrease of half widths of Gaussian filter used to smooth kernels (from 30 km to 10 km). (b) Histograms showing comparison for travelttime misfits for M00 (blue bars) and the final model after 14 iterations (open red bars).

Figure 7 shows an example of the REGFs and the two SGFs computed based on the initial and final models for the station pair K006–K045, K006–K049 (marked as the purple triangles in Figure 1), where significant improvement on SGF-REGF travelttime fits can be observed.

In Figure 8, we show the comparison between the original model (Figure 8b) from Fang et al. (2010), which was smoothed and used as the initial model for this inversion (Figure 8c), and the final shear wave speed model after 14 iterations (Figure 8d), while the topography along the linear array is plotted for reference

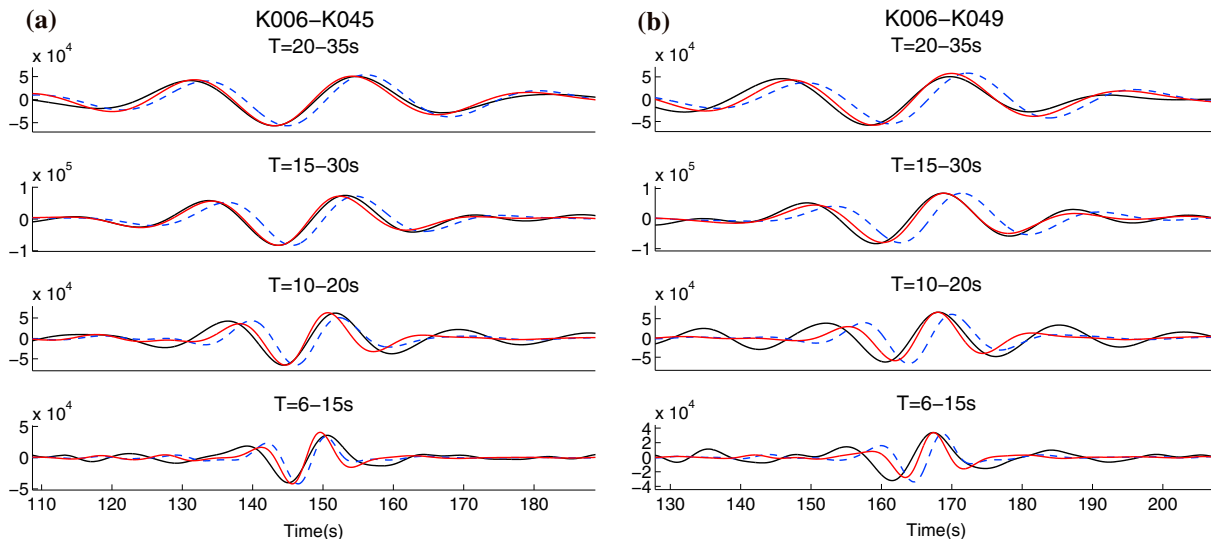


Figure 7. The reconstructed EGFs (black solid line) from station pair (a) K006–K045 and (b) K006–K049 are shown together with the SGFs of the initial (blue dashed line) and final (red solid line) models, respectively.

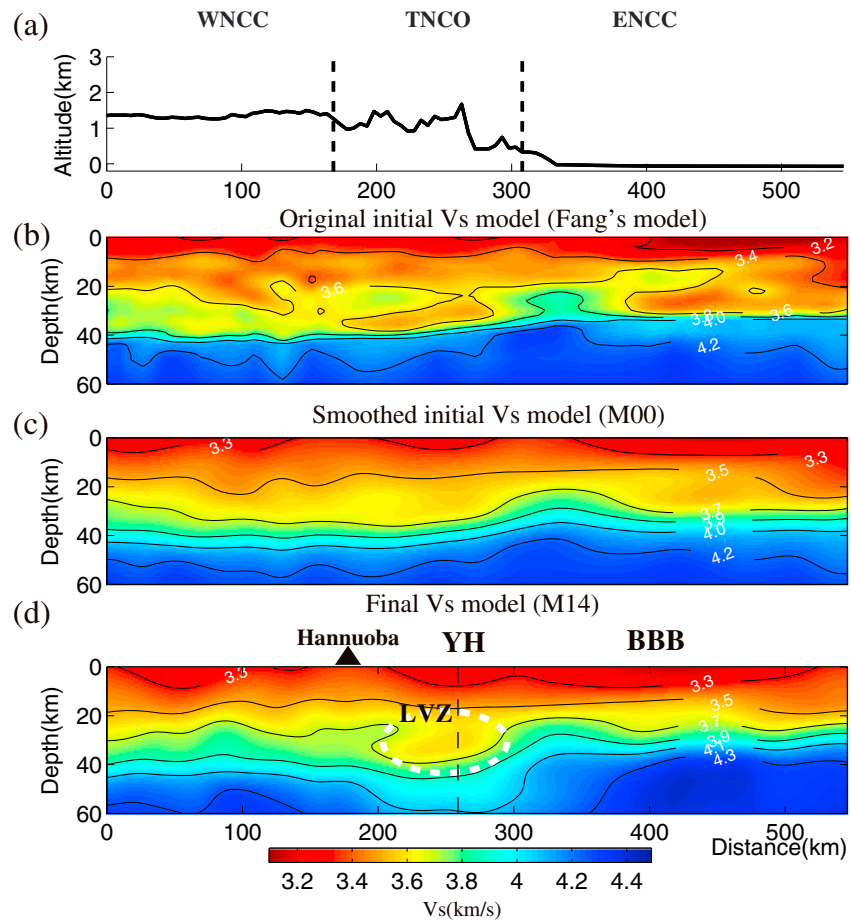


Figure 8. (a) Topography along the linear array, which is incorporated in SEM mesh with 2 km variation from the WNCC to the ENCC. (b) Original Vs model by ambient noise tomography (Fang et al., 2010). (c) Smoothed initial Vs model (M00) and (d) Final Vs model (M14). The white dashed circle marks the prominent low-velocity anomaly. The black triangle marks the location of Hannuoba. YH and BBB are abbreviations of Yanqing-Huailai Basin and Bohai Bay Basin, respectively, which are also shown in Figure 1. The dashed line in Figure 8d shows the location of the vertical shear wave speed profile in Figure S4.

(Figure 8a). For the final model, the large Mesozoic-Cenozoic Bohai Bay Basin (BBB) in the ENCC and Cenozoic intermountain basins including Yanqing-Huailai Basin (YH) in TNCO is clearly outlined with low velocity between 3.2 km/s and 3.3 km/s in the uppermost crust. In general, the S wave velocity map at shallow depth correlates very well with the known surface geological structures. The thickness of crust in the WNCC is larger than that in the ENCC, similar as the initial model.

In comparison with the initial model, two new features are revealed in the final model (Figure 8d), including a striking low-velocity zone (LVZ) in the lower crust, and the very gradual velocity increase close to the depths where the Moho is expected (at distance \sim 200–300 km; Figure 8d) in contrast to the sharp velocity jump across the Moho in either its western (at distance $<$ 200 km) or eastern (at distance $>$ 300 km) segments. As shown in Text S3 and Figure S5, the gradual velocity change across the Moho can be resolved by our data. The LVZ has a horizontal length scale of \sim 80 km and exists in the depth range of 20 to 40 km; the lowest velocity anomaly is about 3.5 km/s. As shown in Figure S4, the shear wave speeds within the LVZ are up to 6.0% lower than that of the initial model and \sim 8.0% lower than the average shear wave speed, indicating that partial melting is likely to exist at these depths. Using the relationship between partial derivative of shear wave speed with respect to melt fraction: $d\ln V_S/dF = -7.9$ (Hammond & Humphreys, 2000) gives us an \sim 1.0% melt fraction. The Moho to its west is relatively deeper than the Moho to its east. Although the model by Fang et al. (2010) (Figure 8a) showed a similar low-velocity zone with a length scale about 130 km in the lower crust in a similar location as ours, their model did not reveal the very gradual velocity increase around the

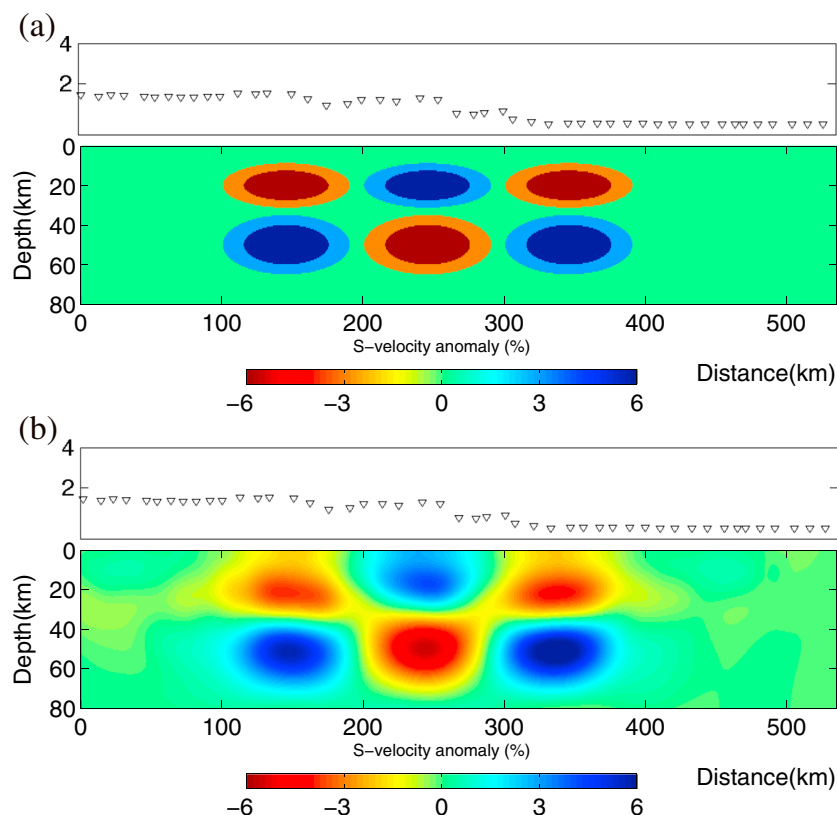


Figure 9. 2-D checkerboard test results: (a) a synthetic 2-D checkerboard model of shear wave speed anomalies in percentage with the colorbar given at the bottom; (b) recovered model after 14 iterations of adjoint tomography. The triangles on the top of model mark the location of the stations.

Moho depth, probably due to the prescribed velocity jump around the Moho interface in their 1-D initial model for dispersion-based inversion. The ability in resolving such small-scale features are most likely owing to the full-wave propagation effect captured by the numerical simulations in adjoint tomography, in contrast to the simple layered model assumption in classical surface-wave tomography. In the following paragraphs, we will focus on understanding the resolution of new features revealed by the final model and discuss their tectonic implications.

To investigate the resolution of our inversions, we also perform 2-D checkerboard tests (Figure 9). The true checkerboard pattern contains two rows of elliptical-shaped anomalies with alternating signs extending from the crust into the uppermost mantle. Every ellipse includes a more enhanced anomaly at the center. All ellipses have major axis length of 80 km, while the length of minor axis is changed from 20 km (inner enhanced region to be 15 km) in the upper row to 30 km (inner enhanced region to be 20 km) in the lower row. These different sizes are designed to assess spatial resolutions of the varying lengths. A homogeneous model is given as the initial model, and synthetic data are generated by the same source-receiver distribution as for the real data and are inverted using the method described above (section 4). The results suggest that structures of these sizes can be well resolved in regions where the data coverage is comparatively good (Figure 9b).

6. Discussions

6.1. Different Initial Models

In order to further test the impact of initial model selection on the final model, we start the adjoint tomographic inversion with an initial model constructed from HBCrust1.0 (Duan et al., 2016) (Figure 10a). This is originally a compressional wave speed model constructed by the wide-angle reflection/refraction method,

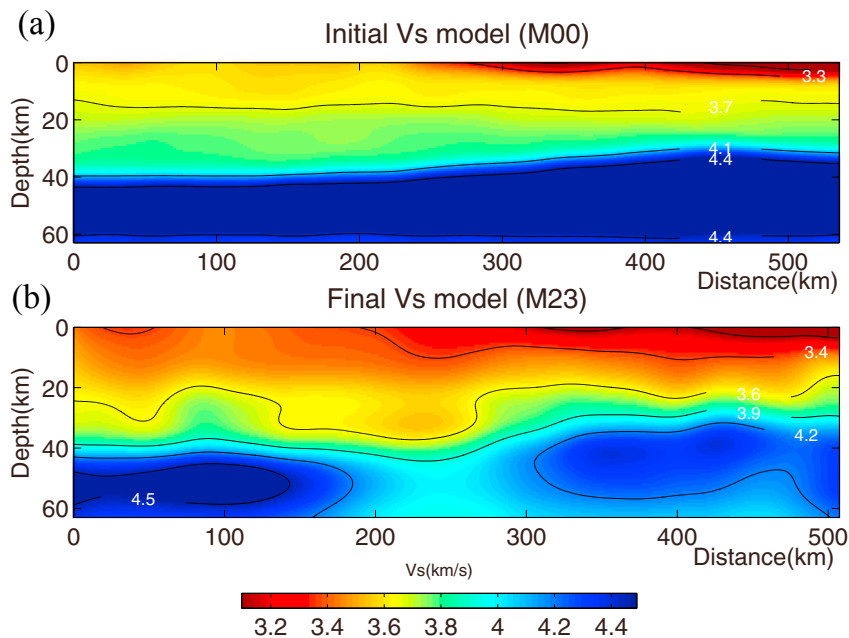


Figure 10. Images show (a) Vs model derived from Duan's Vp model as an alternative initial model M23_Duan_init (Duan et al., 2016) and (b) Final Vs model M23_Duan_final, inverted after 23 iterations.

which is then scaled to a shear wave speed model, M23_Duan_initial. Also note that M23_Duan_initial is much smoother than the Fang's model in section 5 (Figure 8b). We compare the quality of these two different initial models based on the traveltime misfit histograms (Figure S6), which indicate that Fang's model is clearly better than Duan's model as the initial model. We still apply our adjoint tomography procedures to obtain the final model M23_Duan_final after 23 iterations. Compared with the M14_Fang_final model (Figure 8d), M23_Duan_final shows similar and robust features of low wave speed zones in the lower crust and gradual velocity changes across the Moho beneath the junction of Taihang Mountains and Yin-Yan Mountains (Figure 10b). Small-scale differences of the two final models do exist, which are most likely the effect of different initial models used in the inversion.

As Fang's shear wave speed model (Figure 8b) is obtained by a two-step method of ambient noise tomography using dispersion measurements, which may generate unreliable anomalies in the model from fitting the pointwise dispersion curves. Since we derive Duan's shear wave speed model from its original compressional wave speed model by the equation (6), it is not surprising that the derived Vs model, M23_Duan_initial, is much faster than the real structure according to the traveltime misfit histogram in Figure S6b and the low-velocity basin in ENCC appears much thinner than Fang's model. In comparison, our final model (Figure 10b) by adjoint tomography can fit the REGFs much better and reveal some reliable and distinct features that do not exist in either initial model.

6.2. Effect of Different Travelttime Measurements

We also test the effect of using other type of measurements, such as cross-correlation travelttime, instead of multitaper measurements in the inversion. We generate adjoint sources for cross-correlation measurements made on REGFs and SGFs filtered through six overlapping period bands: 6–10 s, 8–15 s, 10–20 s, 15–25 s, 20–30 s, and 25–35 s. Following the same inversion procedures, we obtain a final model (Figure 11) that is very similar to the model based on the multitaper measurements (Figure 8d). This also demonstrates that our inversion strategy is quite stable with respect to different ways of travelttime measurements.

6.3. 2.5-D Assumption in Data Transformation

The 3-D/2-D data transformation is critical for obtaining the REGFs for our inversion strategy. The derivation of this transformation is based on the 2.5-D model instead of the real 3-D model (Forbriger et al., 2014). Also, our benchmark test is also based on a 2.5-D model (Figure S2). However, since the real structure of

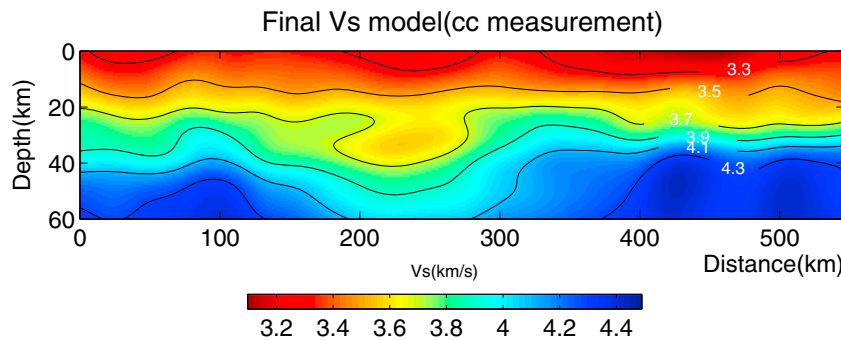


Figure 11. Final Vs model using cross-correlation traveltimes in multiple overlapping period bands instead of multitaper traveltimes.

NCC is probably fairly close to 2.5-D along the linear receiver array, this assumption may hold well for this area and permit the application 2-D adjoint tomography that significantly decreases the computational cost and allows it to be performed on a small cluster (fewer than 200 cores) within several hours (see details in Table 1). Due to 3-D structural heterogeneities, surface wave raypaths between virtual source and receiver pairs may be off great circle paths, that is, not along the direction of the linear array. This may also introduce some slight errors on the final tomographic models, which cannot be modeled in our current 2-D adjoint tomography.

6.4. Effects From Uneven Noise Source Distribution

In this study the Rayleigh wave EGFs retrieved from ambient noise are regarded as the real GFs. However, this does not hold when noise source distribution is heterogeneous in space. Previous studies suggested that the traveltimes (or phase) bias caused by uneven distribution of noise sources is typically less than 1% of the actual traveltimes (e.g., Froment et al., 2010; Harmon et al., 2010; Yao & van der Hilst, 2009) if noise source energy varies smoothly with respect to azimuth. Since in this study we used about 2 year continuous data for ambient noise cross correlation, we think that the noise energy distribution is azimuthally smooth and the phase bias of our retrieved Rayleigh wave EGFs should be mostly less than 1% or even smaller. Therefore, the obtained 2-D velocity model in this study should not be much affected by the uneven noise source distribution.

6.5. Tectonic Implication of Inversion Results

The resolved new structural features beneath the junction of Taihang Mountains and Yin-Yan Mountains (Figure 8d) are roughly spatially correlated with the region where thick (up to ~10 km) crust-mantle transition zone was reported (Zheng et al., 2008). Petrological and geochemical observations on basalt-bearing xenoliths in the Hannuoba area (see Figure 1 for its location) also reported intermixed compositions of spinel lherzolites and mafic granulites at consistent depths of ~30–42 km (Chen et al., 2001) with seismological constraints (e.g., Zheng et al., 2008), implying the possible intense crust-mantle thermo-chemical interactions. Furthermore, the 3-D conductivity model revealed a significant conductive body extending into the mantle between the Hannuoba area and the Datong volcanoes possibly due to partially molten materials, which branches north to the Hannuoba basalts field and thus causes high-conductivity anomalies in the lowermost crust (Zhang et al., 2016). Also, it correlates with regions of high surface heat flow values (Hu et al., 2000). The distinct changes in radial anisotropy from negative in the middle crust to positive in the lower crust where the low-velocity anomaly exists in the Fenhe Graben and Taihang Mountain (Cheng et al., 2012; Fu et al., 2015) also suggest that partial melting is present in the lithosphere due to asthenospheric mantle upwelling and horizontal flow pull. These features are probably associated with both tectonic extension and magmatic underplating during the Mesozoic-Cenozoic uneven lithospheric reactivation and modification.

According to the previous evidences, we propose a possible mechanism to explain the LVZ in the lower crust and very gradual crust-mantle transition zone beneath the northern TNCO region. This mechanism mainly involves thermo-chemical interactions between mantle-derived upwelling melts and the lower crust. The lithosphere of TNCO has been underplated by the upwelling asthenospheric mantle, which caused

significant partial melting. Due to a relative compressive or weakly extensional state of the TNCO lithosphere, the upwelling melts were partially retained in the crust-mantle transition zone instead of all migrating upward to the surface or forming magma chambers to erupt to the surface. This process resulted in mixing of mantle material with lower crustal material, significant thickening of the lower crust as well as parting melting in the lower crust. It probably also reflects a multiphase reworking of preexisting weak zones in the TNCO by a succession of tectonic events since the amalgamation of the NCC. The far-field effects of both Pacific plate subduction and the India-Eurasia collision may result in the latest Cenozoic lithospheric modification.

7. Conclusions

In this study, we perform 2-D ambient noise adjoint tomography for a linear seismic array across the North China Craton (NCC). We apply a 3-D/2-D transformation method used in shallow-seismic Rayleigh wave exploration to the retrieved empirical Green's functions from ambient noise data, which accounts for the effect of different geometrical spreading between the 3-D field data and 2-D synthetic data in our 2-D inversion scheme. Based on a preconditioned conjugate gradient method, we construct a shear wave speed model along the linear array. In comparison with images from the traditional ambient noise tomography, our final model reveals two new distinct features, including a striking low-velocity zone in the lower crust and a gradual velocity change across the Moho beneath the junction of Taihang Mountains and Yin-Yan Mountains in the TNCO, which coincide with possible regions of intense crust-mantle interactions identified by previous studies. A possible mechanism to explain these features mainly involves thermo-chemical interactions between mantle-derived upwelling melts and the lower crust.

The workflow we set up to use recordings of ambient noise data for linear arrays is computationally efficient. This 2-D adjoint tomography scheme presents an important innovative tool to map structures beneath linear arrays, complementary to traditional receiver-function type of analysis. It also paves the way for joint inversions of ambient noise data and scattered waves (Tong et al., 2014) based on the framework of adjoint tomography for both final-scale V_p and V_s crustal structures using linear seismic array recordings.

Acknowledgments

We appreciate constructive comments from the Editor, the Associate Editor, and two anonymous reviewers, which help to improve our original manuscript paper. The waveform data were provided by China Seismic Array Data Management Center at Institute of Geophysics, China Earthquake Administration. The open source spectral-element software package *SPECFEM2D* used for this article is freely available via the Computational Infrastructure for Geodynamics (CIG), and the software package *louis* used for 3-D/2-D spreading transformation is freely available via <http://www.open-toast.de>. We thank Ping Tong and Youyi Ruan for helpful discussions on adjoint tomography. This work is supported by the National Natural Science Foundation of China (grant 41574034) and National Key R&D Program of China (2016YFC0600301). C. Zhang is supported by the China Scholarship Council under grant 201506340102. Computations were performed on the Sandy bridge supercomputer at the SciNet HPC Consortium. SciNet is funded by the Canada Foundation for Innovation under the auspices of Compute Canada, the Government of Ontario, Ontario Research Fund—Research Excellence, and the University of Toronto. Q. Liu also recognizes support from the NSERC Discovery grant 487237. Our final model, data, and computer codes are available from https://github.com/ustcchaozhang/2DNoise_Adjoint_tomography.

References

- Bensen, G. D., Ritzwoller, M. H., Barmin, M. P., Levshin, A. L., Lin, F., Moschetti, M. P., ... Yang, Y. (2007). Processing seismic ambient noise data to obtain reliable broad-band surface wave dispersion measurements. *Geophysical Journal International*, 169, 1239–1260.
- Bozdag, E., Peter, D., Lefebvre, M., Komatitsch, D., Tromp, J., Hill, J., ... Pugmire, D. (2016). Global adjoint tomography: first-generation model. *Geophysical Journal International*, 207, 1739–1766.
- Brocher, T. M. (2005). Empirical relations between elastic wavespeeds and density in the Earth's crust. *Bulletin of the Seismological Society of America*, 95(6), 2081–2092.
- Carlson, R. W., Pearson, D. G., & James, D. E. (2005). Physical, chemical, and chronological characteristics of continental mantle. *Reviews of Geophysics*, 43, RG1001. <https://doi.org/10.1029/2004RG000156>
- Chen, L. (2010). Concordant structural variations from the surface to the base of the upper mantle in the North China Craton and its tectonic implications. *Lithos*, 120(1), 96–115.
- Chen, M., Huang, H., Yao, H., van der Hilst, R. D., & Niu, F. (2014). Low wave speed zones in the crust beneath SE Tibet revealed by ambient noise adjoint tomography. *Geophysical Research Letters*, 41, 334–340. <https://doi.org/10.1002/2013GL058476>
- Chen, M., Niu, F., Liu, Q., Tromp, J., & Zheng, X. (2015). Multi-parameter adjoint tomography of the crust and upper mantle beneath East Asia —Part I: Model construction and comparisons. *Journal of Geophysical Research: Solid Earth*, 120, 1762–1786. <https://doi.org/10.1002/2014JB011638>
- Chen, M., Niu, F., Tromp, J., Lenardic, A., Lee, C. T., Rong, W., & Ribeiro, J. (2017). Lithospheric foundering and underthrusting imaged beneath Tibet. *Nature Communications*, 8, 15659.
- Chen, S., O'Reilly, S. Y., Zhou, X., Griffin, W., Zhang, G., Sun, M., ... Zhang, M. (2001). Thermal and petrological structure of the lithosphere beneath Hannuoba, Sino-Korean Craton, China: Evidence from xenoliths. *Lithos*, 56, 267–301.
- Cheng, C., Chen, L., Yao, H., Jiang, M., & Wang, B. (2012). Distinct variations of crustal shear wave velocity structure and radial anisotropy beneath the North China Craton constrained from ambient noise analysis. *Gondwana Research*, 23, 25–38.
- ChinArray (2006). China Seismic Array waveform data. *China Earthquake Administration*. <https://doi.org/10.12001/ChinArray.Data>
- Covellone, B. M., Savage, B., & Shen, Y. (2015). Seismic wave speed structure of the Ontong Java Plateau. *Earth and Planetary Science Letters*, 420, 140–150.
- Crase, E., Pica, A., Noble, M., McDonald, J., & Tarantola, A. (1990). Robust elastic nonlinear waveform inversion: Application to real data. *Geophysics*, 55, 527–538.
- Dokter, E., Köhn, D., Wilken, D., & Rabbel, W. (2014). Application of elastic 2D waveform inversion to a near surface SH-wave dataset, Presented at the 76th Annual International Conference and Exhibition, EAGE, Extended Abstracts.
- Duan, Y. H., Wang, F. Y., Zhang, X. K., Lin, J. Y., Liu, Z., Liu, B. F., ... Wei, Y. B. (2016). Three-dimensional crustal velocity structure model of the middle-eastern north China Craton (HBCrust1.0). *Science China Earth Sciences*, 59(7), 1477–1488.
- Fan, W. M., Zhang, H. F., Baker, J., Jarvis, K. E., Mason, P. R. D., & Menzies, M. A. (2000). On and off the North China Craton: where is the Archaean keel? *Journal of Petrology*, 41(7), 933–950.
- Fang, H., Yao, H., Zhang, H., Huang, Y.-C., & van der Hilst, R. D. (2015). Direct inversion of surface wave dispersion for three-dimensional shallow crustal structure based on ray tracing: Methodology and application. *Geophysical Journal International*, 201(3), 1251–1263.

- Fang, L., Wu, J., Ding, Z., Wang, W., & Panza, G. F. (2010). Crustal velocity structures beneath North China revealed by ambient noise tomography. *Earthquake Science*, 23, 477–486.
- Fichtner, A., & Villaseñor, A. (2015). Crust and upper mantle of the western Mediterranean—Constraints from full-waveform inversion. *Earth and Planetary Science Letters*, 428, 52–62.
- Fichtner, A., Kennett, B. L. N., Igel, H., & Bunge, H.-P. (2009). Full seismic waveform tomography for upper-mantle structure in the Australasian region using adjoint methods. *Geophysical Journal International*, 179, 1703–1725.
- Fichtner, A., Kennett, B. L. N., Igel, H., & Bunge, H.-P. (2010). Full waveform tomography for radially anisotropic structure: New insights into present and past states of the Australasian upper mantle. *Earth and Planetary Science Letters*, 290, 270–280.
- Forbriger, T., Groos, L., & Schäfer, M. (2014). Line-source simulation for shallow-seismic data — Part 1: Theoretical background. *Geophysical Journal International*, 198, 1387–1404.
- Froment, B., Campillo, M., Roux, P., Gouédard, P., Verdel, A., & Weaver, R. L. (2010). Estimation of the effect of nonisotropically distributed energy on the apparent arrival time in correlations. *Geophysics*, 75, SA85–SA93.
- Fu, Y. V., Gao, Y., Li, A., & Shi, Y. (2015). Lithospheric shear wave velocity and radial anisotropy beneath the northern part of North China from surface wave dispersion analysis. *Geochemistry, Geophysics, Geosystems*, 16, 2619–2636. <https://doi.org/10.1002/2015GC005825>
- Gao, H., & Shen, Y. (2014). Upper mantle structure of the Cascades from full-wave ambient noise tomography: Evidence for 3D mantle upwelling in the back-arc. *Earth and Planetary Science Letters*, 390, 222–233.
- Gao, H., & Shen, Y. (2015). A Preliminary Full-Wave Ambient-Noise Tomography Model Spanning from the Juan de Fuca and Gorda Spreading Centers to the Cascadia Volcanic Arc. *Seismological Research Letters*, 86(5), 1253–1260.
- Gao, S., Rudnick, R. L., Yuan, H. L., Liu, X. M., Liu, Y. S., Xu, W. L., & Wang, Q. H. (2004). Recycling lower continental crust in the North China craton. *Nature*, 432(7019), 892–897.
- Griffin, W. L., Andi, Z., O'Reilly, S. Y., & Ryan, C. G. (1998). Phanerozoic evolution of the lithosphere beneath the Sino Korean craton. In M. F. J. Flower, S.-L. Chung, C.-H. Lo, & T.-Y. Lee (Eds.), *Mantle dynamics and plate interactions in East Asia, Geodynamics Series* (Vol. 27, pp. 107–126). Washington, DC: American Geophysical Union.
- Groos, L. (2013). 2D full waveform inversion of shallow seismic Rayleigh waves, PhD thesis, Karlsruhe Institute of Technology.
- Groos, L., Schäfer, M., Forbriger, T., & Bohlen, T. (2017). Application of a complete workflow for 2D elastic full-waveform inversion to recorded shallow-seismic Rayleigh waves. *Geophysics*, 82(2), R109–R117.
- Hammond, W. C., & Humphreys, E. D. (2000). Upper mantle seismic wave velocity: Effects of realistic partial melt geometries. *Journal of Geophysical Research*, 105(B5), 10,975–10,986. <https://doi.org/10.1029/2000JB900041>
- Harmon, N., Rychert, C., & Gerstoft, P. (2010). Distribution of noise sources for seismic interferometry. *Geophysical Journal International*, 183, 1470–1484.
- Hu, S., He, L., & Wang, J. (2000). Heat flow in the continental area of China: A new data set. *Earth and Planetary Science Letters*, 179(2), 407–419.
- Huang, Y.-C., Yao, H., Huang, B.-S., van der Hilst, R. D., Wen, K.-L., Huang, W.-G., & Chen, C.-H. (2010). Phase velocity variation at periods of 0.5–3 seconds in the Taipei Basin of Taiwan from correlation of ambient seismic noise. *Bulletin of the Seismological Society of America*, 100, 2250–2263.
- Jiang, M., Ai, Y., Chen, L., & Yang, Y. (2013). Local modification of the lithosphere beneath the central and western North China Craton: 3-D constraints from Rayleigh wave tomography. *Gondwana Research*, 24(3), 849–864.
- Komatitsch, D., Liu, Q., Tromp, J., Suss, P., Stidham, C., & Shaw, J. H. (2004). Simulations of ground motion in the Los Angeles Basin based upon the Spectral-Element Method. *Bulletin of the Seismological Society of America*, 94, 187–206.
- Komatitsch, D., & Tromp, J. (2002a). Spectral-element simulations of global seismic wave propagation—I. Validation. *Geophysical Journal International*, 149, 390–412.
- Komatitsch, D., & Tromp, J. (2002b). Spectral-element simulations of global seismic wave propagation—II. Three-dimensional models, oceans, rotation and self-gravitation. *Geophysical Journal International*, 150, 303–318.
- Li, C., Yao, H., Fang, H., Huang, X., Wan, K., Zhang, H., & Wang, K. (2016). 3D near-surface shear-wave velocity structure from ambient-noise tomography and borehole data in the Hefei urban area, China. *Seismological Research Letters*, 87(4), 882–892.
- Lin, F.-C., Li, D., Clayton, R. W., & Hollis, D. (2013). High-resolution 3D shallow crustal structure in Long Beach, California: Application of ambient noise tomography on a dense seismic array. *Geophysics*, 78(4), Q45–Q56.
- Lin, F.-C., Moschetti, M. P., & Ritzwoller, M. H. (2008). Surface wave tomography of the western United States from ambient seismic noise: Rayleigh and Love wave phase velocity maps. *Geophysical Journal International*, 173, 281–298.
- Liu, Q., & Gu, Y. J. (2012). Seismic imaging: From classical to adjoint tomography. *Tectonophysics*, 566–567, 31–66.
- Liu, Q., & Tromp, J. (2006). Finite-frequency kernels based on adjoint methods. *Bulletin of the Seismological Society of America*, 96, 2383–2397.
- Liu, Q., & Tromp, J. (2008). Finite-frequency sensitivity kernels for global seismic wave propagation based upon adjoint methods. *Geophysical Journal International*, 174(1), 265–286.
- Liu, Y., Niu, F., Chen, M., & Yang, W. (2017). 3-D crustal and uppermost mantle structure beneath NE China revealed by ambient noise adjoint tomography. *Earth and Planetary Science Letters*, 461, 20–29.
- Luo, Y. (2012). Seismic imaging and inversion based on spectral-element and adjoint methods, PhD thesis, Princeton University.
- Maggi, A., Tape, C., Chen, M., Chao, D., & Tromp, J. (2009). An automated time-window selection algorithm for seismic tomography. *Geophysical Journal International*, 178, 257–281.
- Menzies, M. A., Fan, W., & Zhang, M. (1993). Palaeozoic and Cenozoic lithoprobes and the loss of > 120 km of Archaean lithosphere, Sino-Korean craton, China. *Geological Society, London, Special Publications*, 76(1), 71–81.
- Nocedal, J. (1980). Updating quasi-Newton matrices with limited storage. *Mathematics of Computation*, 35, 773–782.
- Nuber, A., Manukyan, E., & Maurer, H. (2015). Enhancement of near-surface elastic full waveform inversion results in regions of low sensitivities. *Journal of Applied Geophysics*, 122, R192–R201.
- Pica, A., Diet, J. P., & Tarantola, A. (1990). Nonlinear inversion of seismic reflection data in laterally invariant medium. *Geophysics*, 55, 284–292.
- Ren, J., Tamaki, K., Li, S., & Junxia, Z. (2002). Late Mesozoic and Cenozoic rifting and its dynamic setting in Eastern China and adjacent areas. *Tectonophysics*, 344(3), 175–205.
- Romdhane, G., Grandjean, G., Brossier, R., Rejiba, F., Operto, S., & Virieux, J. (2011). Shallow-structure characterization by 2D elastic full-waveform inversion. *Geophysics*, 76(3), R81–R93.
- Roux, P., Sabra, K. G., Kupperman, W. A., & Roux, A. (2005). Ambient noise cross correlation in free space: Theoretical approach. *The Journal of the Acoustical Society of America*, 117, 79–84.
- Savage, B., Covellone, B. M., & Shen, Y. (2017). Wave speed structure of the eastern North American margin. *Earth and Planetary Science Letters*, 459, 394–405.

- Schäfer, M., Groos, L., Forbriger, T., & Bohlen, T. (2014). Line-source simulation for shallow-seismic data. Part 2: Full-waveform inversion—A synthetic 2D case study. *Geophysical Journal International*, 198, 1405–1418.
- Shapiro, N. M., Ritzwoller, M. H., Molnar, P., & Levin, V. (2004). Thinning and flow of Tibetan crust constrained by seismic anisotropy. *Science*, 305, 233–236.
- Shirzad, T., & Shomali, Z. H. (2014). Shallow crustal structures of the Tehran basin in Iran resolved by ambient noise tomography. *Geophysical Journal International*, 196(2), 1162–1176.
- Simons, F. J., Zielhuis, A., & van der Hilst, R. D. (1999). The deep structure of the Australian continent from surface wave tomography. *Developments in Geotectonics*, 24, 17–43.
- Tape, C., Liu, Q., Maggi, A., & Tromp, J. (2009). Adjoint tomography of the southern California crust. *Science*, 325, 988–992.
- Tape, C., Liu, Q., Maggi, A., & Tromp, J. (2010). Seismic tomography of the southern California crust based on spectral-element and adjoint methods. *Geophysical Journal International*, 180, 433–462.
- Tong, P., Chen, C.-W., Komatsitsch, D., Basini, P., & Liu, Q. (2014). High-resolution seismic array imaging based on an SEM-FK hybrid method. *Geophysical Journal International*, 197, 369–395.
- Tran, K., McVay, M., Faraone, M., & Horhota, D. (2013). Sinkhole detection using 2D full seismic waveform tomography. *Geophysics*, 78(5), R175–R183.
- Tromp, J., Tape, C., & Liu, Q. (2005). Seismic tomography, adjoint methods, time reversal and banana-doughnut kernels. *Geophysical Journal International*, 160, 195–216.
- Weaver, R. L., & Lobkis, O. I. (2004). Diffuse fields in open systems and the emergence of the Green's function (I). *The Journal of the Acoustical Society of America*, 116, 2731–2734.
- Wu, F. Y., Lin, J. Q., Wilde, S. A., Zhang, X. O., & Yang, J. H. (2005). Nature and significance of the Early Cretaceous giant igneous event in eastern China. *Earth and Planetary Science Letters*, 233(1), 103–119.
- Xu, Y. G. (2001). Thermo-tectonic destruction of the Archaean lithospheric keel beneath the Sino-Korean Craton in China: Evidence, timing and mechanism. *Physics and Chemistry of the Earth, Part A: Solid Earth and Geodesy*, 26(9), 747–757.
- Yang, Y., Ritzwoller, M. H., Levshin, A. L., & Shapiro, N. M. (2007). Ambient noise Rayleigh wave tomography across Europe. *Geophysical Journal International*, 168, 259–274.
- Yao, H., Beghein, C., & van der Hilst, R. D. (2008). Surface wave array tomography in SE Tibet from ambient seismic noise and two-station analysis: II. Crustal and upper-mantle structure. *Geophysical Journal International*, 163, 205–219.
- Yao, H., & van der Hilst, R. D. (2009). Analysis of ambient noise energy distribution and phase velocity bias in ambient noise tomography, with application to SE Tibet. *Geophysical Journal International*, 179, 1113–1132.
- Yao, H., van der Hilst, R. D., & de Hoop, M. V. (2006). Surface wave array tomography in SE Tibet from ambient seismic noise and two-station analysis: I. Phase velocity maps. *Geophysical Journal International*, 166, 732–744.
- Zhai, M., & Liu, W. (2003). Palaeoproterozoic tectonic history of the North China craton: A review. *Precambrian Research*, 122(1), 183–199.
- Zhang, H., Huang, Q., Zhao, G., Guo, Z., & Chen, Y. J. (2016). Three-dimensional conductivity model of crust and uppermost mantle at the northern Trans North China Orogen: Evidence for a mantle source of Datong volcanoes. *Earth and Planetary Science Letters*, 453, 182–192.
- Zhao, G., & Liu, W. J. (2001). The formation of granulite and its contribution to evolution of the continental crust. *Acta Petrologica Sinica*, 17(1), 28–38.
- Zhao, G., Sun, M., Wilde, S. A., & Li, S. (2005). Late Archean to Paleoproterozoic evolution of the North China Craton: Key issues revisited. *Precambrian Research*, 136, 177–202.
- Zhao, L., Allen, R. M., Zheng, T., & Hung, S. H. (2009). Reactivation of an Archean craton: Constraints from P and S wave tomography in North China. *Geophysical Research Letters*, 36, L17306. <https://doi.org/10.1029/2009GL039781>
- Zheng, T. Y., Zhao, L., & Zhu, R. X. (2008). Insight into the geodynamics of cratonic reactivation from seismic analysis of the crust–mantle boundary. *Geophysical Research Letters*, 35, L08303. <https://doi.org/10.1029/2008GL033439>
- Zhou, Y., Dahmen, F. A., & Nolet, G. (2004). 3-D sensitivity kernels for surface-wave observables. *Geophysical Journal International*, 158, 142–168.
- Zhu, H., Bozdağ, E., Peter, D., & Tromp, J. (2012). Structure of the European upper mantle revealed by adjoint tomography. *Nature Geoscience*, 5, 493–498.
- Zhu, H., Bozdağ, E., & Tromp, J. (2015). Seismic structure of the European upper mantle based on adjoint tomography. *Geophysical Journal International*, 201, 18–52.
- Zhu, H., & Tromp, J. (2013). Mapping tectonic deformation in the crust and upper mantle beneath Europe and the North Atlantic Ocean. *Science*, 341, 871–875.